Vol.4, No.9, Page 2497- 2507, 2026 https://doi.org/10.59628/jast.v4i9.3282 ISSN 2958-9568 JAST

SUN PUBLISHER

مجلة جامعة صنعاء للعلوم التطبيقية والتكنولوجيا
Sana'a University Journal of Applied Sciences and Technology
https://journals.su.edu.ye/index.php/jast/

Fuzzy Supervisory Tracking Control for a Solar-Tower CSP Plant with an Equivalent-Area Pentagonal Heliostat Field: A Case Study of Al Hudaydah, Yemen

Hajer Ali Al-Maqaleh *, Radwan Al-Bouthigy and Abdul Malik Momin

Department of Mechatronics Engineering, Faculty of Engineering, Sana'a University, Sana'a, Yemen.

*Corresponding author: halmakaleh@gmail.com

Abstract

Heliostat tracking deviation is one of the optical factors that becomes more visible when the performance of a solar-tower CSP plant is examined over a full year. In this paper, a 100 MW molten-salt solar-tower plant with 8 hours of thermal storage in Al Hudaydah, Yemen, was studied. A baseline annual run was generated in SAM, and the 8760 hourly outputs were then used in MATLAB to compare conventional tracking with PID and Mamdani fuzzy supervisory tracking. The angular-error model was not taken from field measurements; it was introduced as a common simulation disturbance so that the three cases could be compared under the same plant data. The PID and fuzzy supervisors were given the same correction limit, and electricity produced from stored heat was kept in the annual output. Since SAM does not directly resolve the pentagonal mirror shape, the field was treated through equivalent area and optical parameters. According to the fuzzy supervisor, the annual results showed that, in the higher energy output, the generation increased from 384.91 GWh to 389.95 GWh. Reaching 388.05 GWh, PID controller main advantage appeared in the tracking-error response as the variation decreased. Accordingly, fuzzy supervision is suitable for annual generation while PID is better for tracking stability.

1. INTRODUCTION

Solar tower concentrated solar power (CSP) plants consist of a heliostat field, central receiver, high-temperature heat transfer fluid, thermal energy storage (TES), and thermodynamic power block. TES allows power generation after sunset and during short periods of reduced irradiance, giving solar-tower plants a dispatchability advantage over non-storage solar technologies [1] , [2]. The performance of the plant is significantly affected by the heliostat field because the radiation captured by the receiver is affected by cosine loss, atmospheric attenuation, shading, blocking, reflectance, surface error, and angular alignment [2–4].

The heliostat geometry and field arrangement are important because they affect the packing density, optical losses, structural behavior, drive requirements, and life cycle cost [3], [4]. For pentagonal heliostats, the idea of a Stellio with a combination of a five-sided concentrator, compact kinematics, and a relatively symmetric support structure was studied [5] . Field-layout research under certain assumptions has reported a small annual intercepted-energy advantage for pentagonal configurations [6]. Wind loads and wind induced deviations of the pentagonal Stellio heliostat have also been studied in full scale measurements and analytical studies [7, 8] The studies confirm the choice of a pentagonal design concept but do not imply that all pentagonal mirrors are superior to square or rectangular mirrors. The performance is a function of the entire structure, field boundary, receiver, drive arrangement, optical quality, and operating conditions.

The variations can be attributed to installation errors, calibration drift, encoder uncertainty, actuator and gearbox limitations, gravity, structural deformation, and wind loading. Small angular misalignments lead to a reduced intercept factor and change in the thermal input into the receiver. In earlier non-review studies, correction strategies for heliostat systems were studied based on feedback and calibration. Chiesi et al. developed a runtime closed-loop approach to identify and correct heliostat tracking errors. Pargmann et al. proposed a hybrid calibration method using real heliostat calibration data by combining robotic rigid body kinematics with neural networks [9, 10] These studies demonstrated the value of developing supervisory tracking strategies that could

©2026 The Author(s). This article is licensed under CC By 4.0

modify the tracking response in a manner to adapt to varying operating conditions.

Heliostat orientation control has been performed using fuzzy logic control in the last decade because it can deal with nonlinear tracking behavior and changing operating conditions without the need for the same amount of parameter tuning as a conventional PID controller [11, 12]. Fuzzy controllers have been used in solar-thermal systems with uncertain and varying operating conditions [13]. The advantage of explicit disturbance handling and mode coordination within the framework of CSP systems is also shown in model predictive control studies [14, 15] Annual controller comparisons should be based on the same operating data, correction authority, and definitions of performance, and should save electricity generated from the stored heat when the solar field is not operating.

The present study compares the conventional, PID and Mamdani fuzzy supervisory tracking using one-year full SAM output for 100 MW solar-tower CSP plant in Al Hudaydah, Yemen. The main contributions are as follows:

- A complete Mamdani controller having three inputs and one output. It contains explicit membership functions and 27 rules.
- PID benchmark for PID control with the same maximum angular error correction gain as before.
- The angular error and Gaussian optical penalty of a telescope are expressed in a unit-consistent form of the synthetic angular error.
- An annual “power correction” process (that) preserves TES, but also allows for the ability to generate storage-only SAMs, as well as to conduct daily statistical analyses using confidence intervals and standardized effect sizes.

The work is limited to plant-level simulation and postprocessing. It is not a measure of the motor-level servo performance, uniformity of the flux on the receiver, or geometric advantage of a pentagonal heliostat.

2. MATERIALS AND METHODS

2.1. Study Framework

The workflow included preparation of the weather data, plant simulation using SAM, hourly output export from SMAP to MATLAB for preprocessing and controller evaluation before post-processing in optical and power, followed by paired daily statistical analysis. The baseline annual plant operation was provided by SAM, and the comparative conventional, PID, and fuzzy supervisory cases were implemented in MATLAB, as illustrated in Fig(1).

2.2. Site, Weather Data, and CSP Plant Model

The case study includes a 100 MW solar power tower facility located in the town of Al Hudaydah in the Al Hudaydah Governorate in southern Yemen at 15.05° N and 43.28° E. Using the NASA POWER data service, 8760 h of solar resource and meteorological data on an hourly time step were provided for the entire year and then converted to a non-leap year weather file [16]. A 100 MW solar power tower facility was modeled in SAM using the molten salt power tower model [17]. The modeled power tower includes a field of heliostats that reflect concentrated solar radiation to a central tower receiver, a hot-salt storage tank, a cold-salt storage tank to absorb heat as it cools, and an 8h thermal storage system. The facility is powered by a 100 MW Rankine-cycle plant that is charged and discharged by hot and cold storage tanks, respectively.
Using the annual electrical energy and time series of electrical power, field thermal power, and field efficiency from the hourly simulation of the baseline system of the case study site, a MATLAB model was set up. The key parameters used in the hourly simulations of the baseline system of the case study site are summarized in Table (1).

2.3. Equivalent-Area Pentagonal Heliostat Representation

The medium-area pentagonal heliostat was maintained as the chosen design concept because of the possible benefits reported in published Stellio studies regarding the full pentagonal structure, kinematics, and field arrangement [5–8] Instead of a direct five-sided optical boundary, this study represented the heliostat conceptually by equivalent SAM dimensions and reflective area, as depicted in Fig. (2). The SAM does not explicitly model an arbitrary five-sided mirror boundary in the heliostat input at the plant level. The concept was expressed in terms of parameters such as equivalent width, height, ratio of reflective area, reflectivity, availability, and optical error.

$$A_{eq} = WHr_A = 12.2 \times 12.2 \times 0.97 = 144.37m^2 \quad (1)$$

where A_{eq} is the equivalent reflective area of one heliostat, W and H are the nominal SAM width and height, respectively, and r_A is the reflective-area ratio.

$$N_h = \frac{A_{field,ref}}{A_{eq}} = \frac{1{,}171{,}601.5}{144.37} \approx 8{,}115. \quad (2)$$

where N_h is the approximate number of heliostats, and $A_{field,ref}$ is the total reflective area of the heliostat field. In this study, a pentagonal heliostat was considered an equivalent-area element in the SAM model. This is sufficient to maintain the reflective area used in the annual plant simulation but should not be confused with a full

©2026 The Author(s). This article is licensed under CC By 4.0

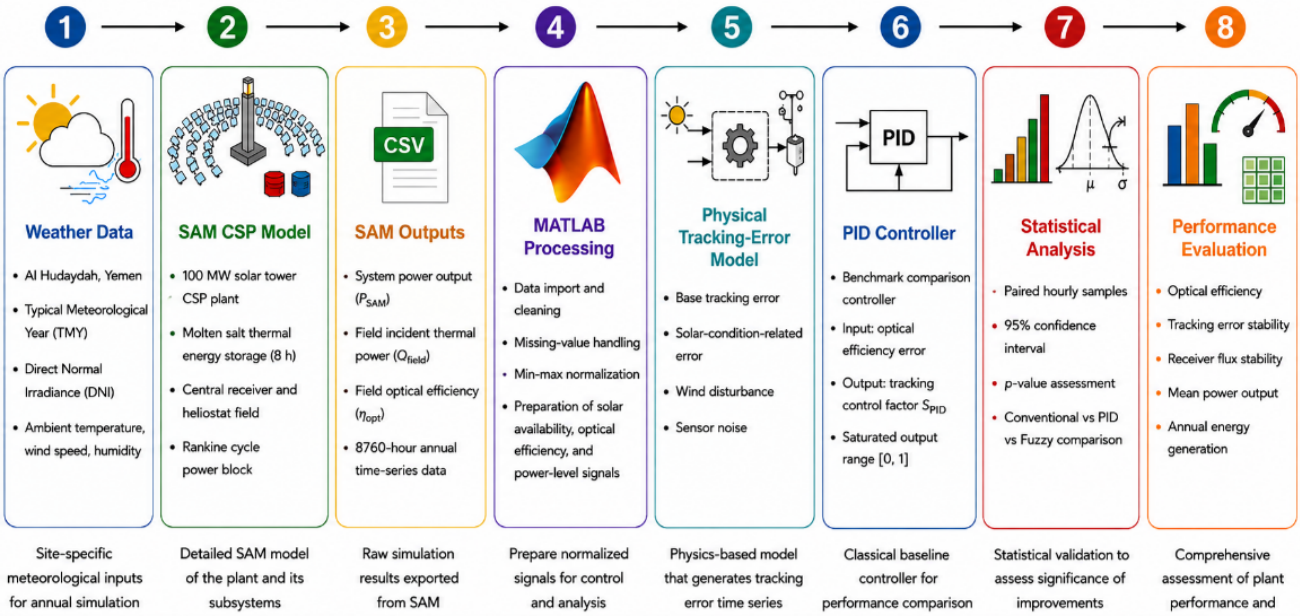


Figure 1. Overall SAM-MATLAB simulation and supervisory-control workflow.

Table[1]: Principal SAM plant and heliostat-field parameters.

Parameter	Value	Parameter	Value
Plant capacity	100 MW	**Storage duration**	8 h
Heliostat width	12.2 m	**Heliostat height**	12.2 m
Reflective-area ratio	0.97	**Equivalent reflective area**	144.37 m^2
Mirror reflectance incl. soiling	0.90	**Total reflective area**	1,171,601.5 m^2
Approx. heliostat count	8,115	**Base solar-field land area**	1,647.59 acres(6.67 km^2)
Total land area	1,692.59 acres(6.85 km^2)	**Design-point DNI**	850 W m^{-2}
Average attenuation loss	8.5%	**Tower height**	188.7 m
Minimum tower distance	141.5 m	**Maximum tower distance**	1,792.3 m
Distance-to-height ratio	0.75–9.5	**Land-area multiplier**	1.0
Field availability	0.95	**Constant field loss**	5.0%

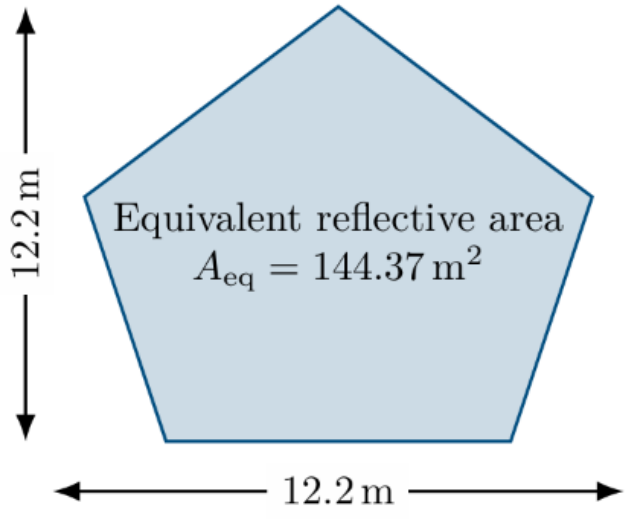


Figure 2. A pentagonal heliostat (left) and the same heliostat represented by the SAM shape parameters (diameter and area, right).

optical or structural description of the five-sided mirror. This model does not consider the effects that depend on the actual geometry, such as local shading and blocking, cosine behavior, wind loading, structural deformation, and detailed distribution of flux on the receiver. So the presented performance improvements are considered improvements because of the supervisory tracking approach and not as proof that the pentagonal shape is better.

2.4. Data Preprocessing and Operating Masks

All time series (output from the simulation) were inspected for missing values or values that were not physically realistic. For nighttime hours or hours when the plant was off, the respective values were set to zero. Optical efficiency was kept between 0 and 1. All three input values to the controller were then normalized to their respective annual minimum and maximum values

©2026 The Author(s). This article is licensed under CC By 4.0

(e.g., for ambient temperature, for irradiance, etc.).

$$S_A(t) = \frac{Q_{field}(t) - Q_{min}}{Q_{max} - Q_{min}} \quad (3)$$

where $S_A(t)$ is the normalized solar availability, $Q_{field}(t)$ is the field incident thermal power, and Q_{min} and Q_{max} are the annual minimum and maximum values, respectively.

$$S_\eta(t) = \frac{\eta_{conv}(t) - \eta_{min}}{\eta_{max} - \eta_{min}} \quad (4)$$

where $S_\eta(t)$ is the normalized optical efficiency, $\eta_{conv}(t)$ is the baseline SAM optical efficiency, and η_{min} and η_{max} are its annual limits.

$$S_P(t) = \frac{P_{SAM}(t) - P_{min}}{P_{max} - P_{min}} \quad (5)$$

where $S_P(t)$ is the normalized plant power, $P_{SAM}(t)$ is the baseline electrical output, and P_{min}- $P_{max}$are are the annual limits.

This condition must be met for two different cases:

1) hours when the solar field is active (solar field active hours), and during these hours, both the incident field thermal power and optical efficiency must be greater than zero.

2) hours when the solar field is generating power (power generating hours), and during these hours the SAM electrical output must be greater than zero. The power correction due to tracking was therefore calculated for both cases above, and the correct SAM output (which is the stored heat generated by the solar field during the hours that it is inactive) was returned for hours when the solar field was inactive.

2.5. Mamdani Fuzzy Supervisory Controller

A Mamdani fuzzy controller was used as the basis for this study. Three inputs, S_A, the supervisory tracking-authority factor; S_η, the longitudinal error; and S_P, the range to the parking bay, were used to produce a single output, S_{fuzzy}, the supervisory tracking-authority factor. S_{PA}, S_η and S_P have three linguistic values, or sets, each: Low, Medium, High. The output, S_fuzzy, also has three linguistic values or sets: Stow, Partial, and Full. Here, Stow denotes the lowest amount of supervisory tracking authority and thus does not equal the calculated parking angle. The numerical partitions for the Low, Medium and High sets for the inputs and the Stow, Partial and Full sets for the output are shown in Figure 3. The membership functions for the Low and High sets of the inputs were chosen to be of the trapezoidal type. The membership function for the medium set of inputs was chosen to be of a triangular type. The parameters for the trapezoidal membership functions for the Low and High sets of the inputs are chosen to be [0,0,0.20,0.40] and [0.60,0.80,1,1] respectively. The parameters for the triangular membership function for the medium set of the inputs were chosen to be [0.25,0.50,0.75]. The method of implication

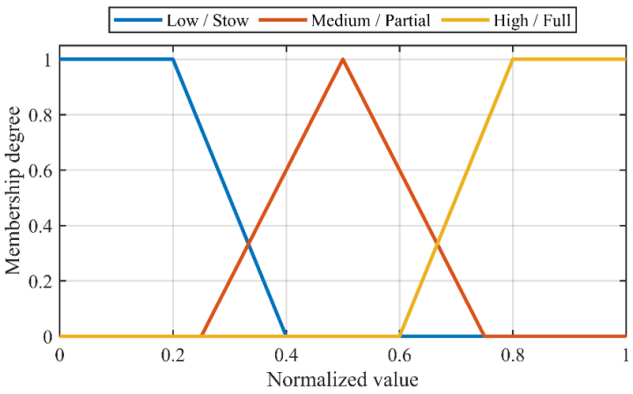


Figure 3. The membership function partitioning for the normalized input and output fuzzy variables.

between the input membership functions and the membership functions for the output membership functions was chosen to be the Mamdani minimum implication. The method of aggregating the membership functions of the rules was chosen to be the maximum aggregation. Centroid defuzzification was chosen as the method of fuzzification of the output variable.

The complete 27-rule base for the supervisory control layer is listed in Table 2. The amount of tracking authority granted by the supervisory control layer increased monotonically with solar availability, optical efficiency, and plant power. Table 2 presents the rule base. The rule base was created by an expert; however, before the rule base could be implemented as a supervisory control layer, it needed to be retuned using data collected at the site.

2.6. Fuzzy Rule Base

The fuzzy rule base was derived from a set of rules that described the behavior of a solar tower CSP power plant. Low solar radiation leads to weak tracking action, whereas high solar radiation and acceptable optical efficiency and power output lead to full tracking correction.

The complete 27-rule base is shown in the following Table (2).

2.7. Simulation-Based Angular-Error Model

A synthetic angular-error signal was created for annual comparison. No mechanical model of the motor was implemented. Each error was converted to milliradians and summed. In all three cases, the manifest realization of the disturbance was identical.

$$e_{conv}(t) = |e_b + e_s(t) + e_w(t) + e_n(t)| \quad (6)$$

where $e_{conv}(t)$ is the conventional angular-error magnitude in mrad, e_b is the baseline term, $e_s(t)$ is the solar availability component, $e_w(t)$ is a periodic wind-related term, and $e_n(t)$ is the random measurement or tracking

©2026 The Author(s). This article is licensed under CC By 4.0

Table[2]: 27-rule Mamdani fuzzy rule base.

Rule	Solar availability	Optical efficiency	Power level	Tracking control
1	Low	Low	Low	Stow
2	Low	Low	Medium	Stow
3	Low	Low	High	Stow
4	Low	Medium	Low	Stow
5	Low	Medium	Medium	Stow
6	Low	Medium	High	Stow
7	Low	High	Low	Partial
8	Low	High	Medium	Partial
9	Low	High	High	Partial
10	Medium	Low	Low	Stow
11	Medium	Low	Medium	Partial
12	Medium	Low	High	Partial
13	Medium	Medium	Low	Partial
14	Medium	Medium	Medium	Partial
15	Medium	Medium	High	Full
16	Medium	High	Low	Partial
17	Medium	High	Medium	Full
18	Medium	High	High	Full
19	High	Low	Low	Partial
20	High	Low	Medium	Partial
21	High	Low	High	Full
22	High	Medium	Low	Partial
23	High	Medium	Medium	Full
24	High	Medium	High	Full
25	High	High	Low	Full
26	High	High	Medium	Full
27	High	High	High	Full

noise.

$$e_s(t) = e_{s,max}\left[1 - S_A(t)\right] \quad (7)$$

where $e_{s,max}$ = 0.5236 mrad is the assumed maximum solar-condition-related error, and $S_A(t)$ is the normalized solar availability.

$$e_w(t) = A_w sin\frac{2\pi t}{24} \quad (8)$$

where A_w = 0.3491 mrad is the assumed wind-related amplitude, and t is the time in hours.

$$e_n(t) \sim N\left(0, \sigma_n^2\right) \quad (9)$$

where $e_n(t)$ is zero-mean Gaussian noise, σ_n= 0.1745 mrad, and the baseline term is e_b = 1.8 mrad.

The image error of the baseline was a parameter in the simulations and not a simulated actuator error. The solar, wind, and noise terms were assumptions typical for comparisons and not real field data.

$$e_{PID}(t) = e_{conv}(t)\left[1 - \gamma S_{PID}(t)\right] \quad (10)$$

where $e_{PID}(t)$ is the PID-adjusted angular error, $S_{PID}(t)$ is the bounded PID supervisory signal, and γ is the maximum fractional correction gain.

$$e_{fuzzy}(t) = e_{conv}(t)\left[1 - \gamma S_{fuzzy}(t)\right] \quad (11)$$

where $e_{fuzzy}(t)$ is the fuzzy-adjusted angular error, and $S_{fuzzy}(t)$ is the bounded fuzzy supervisory signal. The same γ = 0.10 was used for the PID and fuzzy controls.

Several non-review studies have already been presented in the prior work, for instance, regarding the error of a heliostat during its tracking, detection, and correction, as well as the use of this error for an improvement of a heliostat field calibration by using both feedback and data-driven methods. All these studies have been presented in references [9] and [10].

2.8. PID Benchmark

This benchmark compares the normalized with respect to the optical efficiency error PID and fuzzy controllers. Before making the final comparison, a bounded search space for the PID controller gains was performed, and its gains remained constant. It should be noted that the result of the fuzzy controller output was not utilized for tuning the gain in this work. The typical target value for optical efficiency was set as η_{target} = 0.90. For the PID used here, K_p= 0.30, K_i = 0.005, and K_d = 0.05. The integral action was limited to the range [-5, 5], and the controller output was limited to [0, 1]. The PID controller

©2026 The Author(s). This article is licensed under CC By 4.0

was set to zero when the solar field was not functioning.

$$e_\eta(k) = \eta_{target} - S_\eta(k) \quad (12)$$

where $e_\eta(k)$ is the normalized optical efficiency error at sample k, η_{target} is the desired normalized level, and $S_\eta(k)$ is the normalized SAM optical efficiency.

$$S_{PID}(k) = sat_{[0,1]}\left[0.5 + K_p e_\eta(k) + K_i I(k) + K_d \Delta e_\eta(k)\right] \quad (13)$$

where $S_{PID}(k)$ is the bounded PID supervisory signal at sample k, saturated to the interval [0,1]; $e(k) = e_\eta(k)$ is the normalized optical-efficiency error; $I(k) = \sum_{i=1}^{k} e(i)$ is the accumulated error, and $\Delta e(k) = e(k) - e(k-1)$ is the first difference of the error signal.

The PID is an hourly benchmark at the plant level. It is not a second-scale azimuth-elevation servo controller.

2.9. Optical-Efficiency and TES-Preserving Power Calculation

In this study, the SAM software package was used in combination with an equivalent-area heliostat. Five-sided ray tracing for the pentagonal mirror was not performed in this study; the geometry-based advantages of the pentagonal heliostat over the round or rectangular heliostat are not reported here. The additional term in the above equation was added after the annual simulations with SAM (used here as the CSP annual performance simulation environment [18]) were performed. Thus, this term is a simple post-processing term and NOT a SAM equation or a term resulting from shape-based ray-tracing for the pentagonal mirror.

$$I(e) = exp\left[-\left(\frac{e}{\sigma}\right)^2\right] \quad (14)$$

where $I(e)$ is the dimensionless optical penalty, *e* is the angular error in mrad, and σ = 5.091 mrad is an effective reflected-image spread parameter taken from the SAM optical input.

$$\eta_{ideal}(t) = \frac{\eta_{conventional}(t)}{I[e_{conv}(t)]} \quad (15)$$

where $\eta_{ideal}(t)$ is an idealized optical efficiency reference after removing the modeled conventional angular penalty, and $\eta_{conventional}(t)$ is the SAM baseline optical efficiency.

$$\eta_j(t) = \eta_{ideal}(t)\, I\left[e_j(t)\right], j \in \{PID, fuzzy\} \quad (16)$$

where $\eta_j(t)$ is the controller-adjusted optical efficiency, and $e_j(t)$ is the corresponding angular error. Values were limited to [0, 1].

$$P_j(t) = P_{SAM}(t)\, R_j(t) \quad (17)$$

where $P_j(t)$ is the post-processed electrical output, $P_{SAM}(t)$ is the baseline SAM output, and $R_j(t) = \frac{\eta_j(t)}{\eta_{conventional}(t)}$ during active-field generation and $R_j(t)$=1 otherwise.

Equation 17 retains the storage-only SAM generation while the molten salt state of charge and the receiver input for subsequent hours are not updated. This yields an annual TES-preserving post-processing approximation, as opposed to a full optical/TES/power-block simulation.

2.10. Performance Indicators and Statistical Analysis

$$E_{annual} = 10^{-6} \sum_{t=1}^{8760} P(t)\Delta t,\ \Delta t = 1h \quad (18)$$

where E_{annual} is the annual electricity in GWh, $P(t)$ is the hourly electrical output in kW, the sampling interval is 1 h, and 10^{-6} converts kWh to GWh.

$$Q_{rec,j}(t) = Q_{field}(t)\, \eta_j(t) \quad (19)$$

where $Q_{rec,j}(t)$ is estimated receiver thermal input for case j, $Q_{field}(t)$ is SAM field incident thermal power, and $\eta_j(t)$ is case-specific optical efficiency.

The receiver thermal input (BTU/h) time series was normalized by dividing it by the maximum value for each time series (to ensure similarity between the time series). The 24-hour moving average was removed from the time series. The standard deviation of the residuals was calculated to determine the variability in the thermal input time series. This does NOT include spatial information on the receiver fluxes and therefore does NOT show receiver flux uniformity.

$$Improvement\ (\%) = \frac{X_j - X_{conv}}{X_{conv}} \times 100 \quad (20)$$

where X_j is the higher-is-better metric for PID or fuzzy control, and X_{conv} is the corresponding conventional value.

$$\text{Reduction}\ (\%) = \frac{X_{conv} - X_j}{X_{conv}} \times 100 \quad (21)$$

where X_j is a lower-is-better variability metric. A negative result indicates deterioration.

The hourly output of the controller was aggregated to 365 daily pairs of energy and optical efficiency over one year. The energy of a system, including storage, was summed over 24 h, and the optical efficiency of a solar field was averaged over the active hours of solar field tracking. Two-sided paired t-tests were performed to compare PID and fuzzy tracking to fixed tracking at α= 0.05. The corresponding Cohen's d_z effect size was calculated from the t-statistic of the paired-samples t-test divided by the square root of n. Here, all of a controller's outputs are a deterministic transformation of one of the time series outputs by SAM over the year; therefore, statistical significance proves only numerical differences within a year, not experimental verification.

3. RESULTS AND DISCUSSION

©2026 The Author(s). This article is licensed under CC By 4.0

Table[3]: Final annual performance comparison.

Indicator	Conventional	PID	Fuzzy	PID change	Fuzzy change
Mean optical efficiency	0.50581	0.51394	0.51726	+1.61%	+2.27 %
Thermal-input residual std.	0.19866	0.20077	0.20326	-1.06%	-2.32 %
Tracking-error std. (°)	0.01847	0.01744	0.01839	5.58 % reduction	0.42% reduction
Mean generating-hour power (MW)	88.77	89.49	89.93	+0.81%	+1.31 %
Annual energy (GWh)	384.91	388.05	389.95	+0.81%	+1.31%

Note: Negative values in the residual row indicate a decrease or deterioration; positive values in the tracking-error row indicate a percentage reduction.

3.1. Overview of Simulation Results

In this study, the performance of the hybrid sun tracker with fuzzy supervision and PID feedback for fuzzy supervision and PID cases over a full year of simulations is summarized in Table 3. It can be seen that the best performance for the mean optical efficiency, the mean power produced during the generating hours, and the total annual energy is for the fuzzy-supervision case. The PID case exhibited the smallest standard deviation of the tracking error. As expected, none of the control strategies tested were able to decrease the receiver thermal-input residual standard deviation, which was positive for both fuzzy-supervision and PID cases. Negative values in the residual column indicate improvement, while positive values indicate a decrease or deterioration in that variable.

3.2. Optical Efficiency Results

The conventional solution yielded an average optical efficiency of 0.50581. With the use of the PID controller, this figure increased to 0.51394 for the DCS-based solution and 0.51726 for the fuzzy-supervised solution. Thus, the latter of the above solutions revealed the largest rise, specifically 1.61% and 2.27% of increase with respect to the previously specified values. Figures 4a and 4b show the average optical efficiency of all the considered control solutions on a daily basis and on a longer timescale. The fuzzy supervised solution displayed the highest optical efficiency during the active-field time.

3.3. Supervisory Action and Tracking Error

The fuzzy supervisory controller out assigned the tracking authority of the PID controller for the selected time period as illustrated in Figure 5a. This is despite both controllers being assigned the same correction coefficient gamma for the selected interval. Therefore, even though the two controllers were configured to support the same objective, the amount of controller activity was vastly different for the two controllers. It would be useful to include measures of the actuator energy required, the number of actuator movements, and penalties for wear for such a hardware comparison.

The annual tracking-error standard deviation decreased from 0.01847° to 0.01744° with PID tracking. This decrease is by 5.58%. With fuzzy supervision, the tracking error's annual standard deviation is further decreased to 0.01839°. This only corresponds to a 0.42% decrease. The error profiles for PID tracking and fuzzy supervision for the same time interval are shown in Figure 5b. Therefore, although the fuzzy supervised optical and energy estimates were higher than the PID tracking estimates, the PID tracking results in lower annual error variability.

3.4. Power Output and Annual Energy

The mean power for hours when MEELPA generated power increased for the supervising controller from 88.77 MW (PID supervising) to 89.49 MW and then to 89.93 MW (fuzzy supervising), as shown in Fig. 6a. The relative increase in the power generated by the improved supervising controller with respect to the power of a conventional tracker is plotted in Fig. 6b for the same time periods. The fuzzy supervising controller assigns more tracking authority during the day to generate more power.

By enabling the correction of the storage-only generation for the assessment of the overall system performance, the annual energy production was increased from 384.91 GWh by 3.14 GWh yr-1 (0.81%) up to 389.95 GWh yr-1 by the fuzzy-controlled PV-diesel system. This corresponds to an increase of 5.04 GWh yr-1 (1.31%) by the fuzzy control compared with the PID control. The daily and annual energy productions are illustrated in Fig. 7.

3.5. Receiver Thermal-Input Variability

The standard deviation of the receiver thermal-input residuals increased for all control methods. The increase in the standard deviation was from the baseline case value of 0.19866 to 0.20077 for the PID controller case and to 0.20326 for the fuzzy logic controller case, which corresponded to increases of 1.06% and 2.32%, respectively. As shown in Fig. 8, the residual profiles for the

©2026 The Author(s). This article is licensed under CC By 4.0

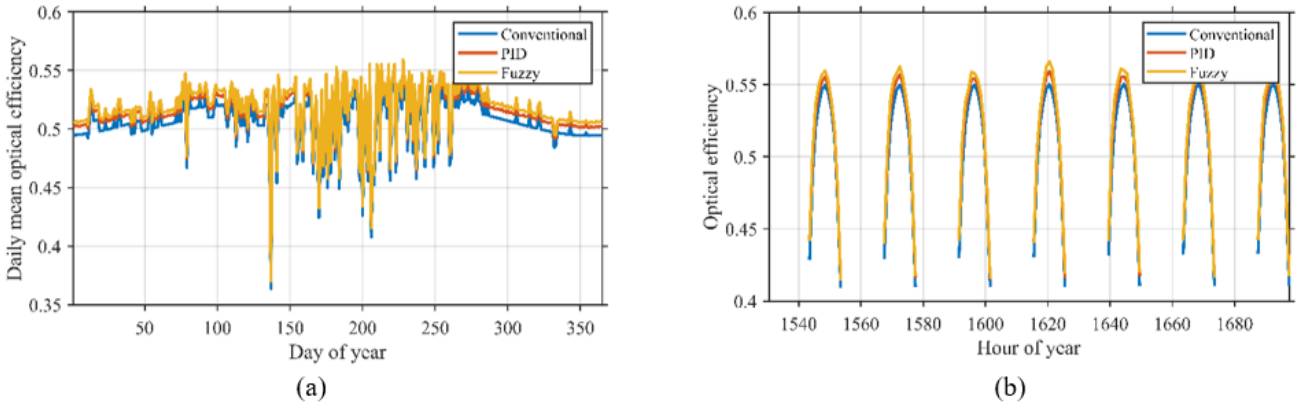


Figure 4. Optical-efficiency during the year: (a) annual averaged and (b) selected operating interval. The selected interval

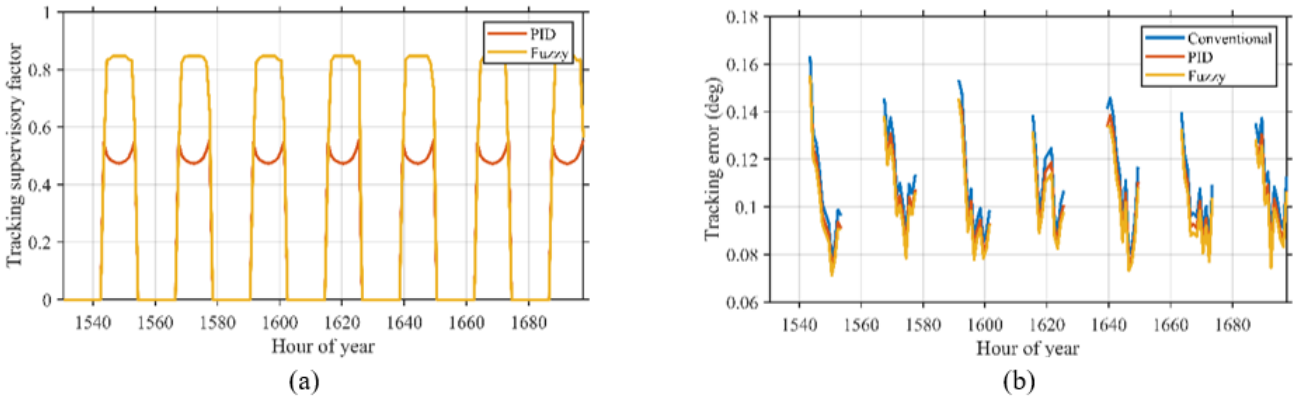


Figure 5. Selected operating intervals: (a) PID and fuzzy supervisory tracking-authority factors and (b) modeled angular

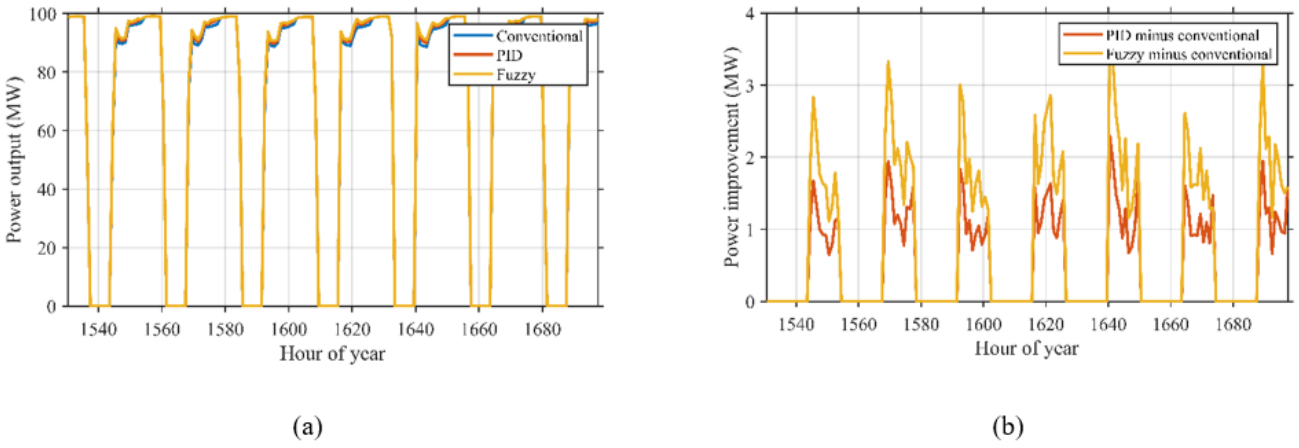


Figure 6. Selected operating intervals: (a) power output and (b) controller-based power increase relative to conventional

©2026 The Author(s). This article is licensed under CC By 4.0

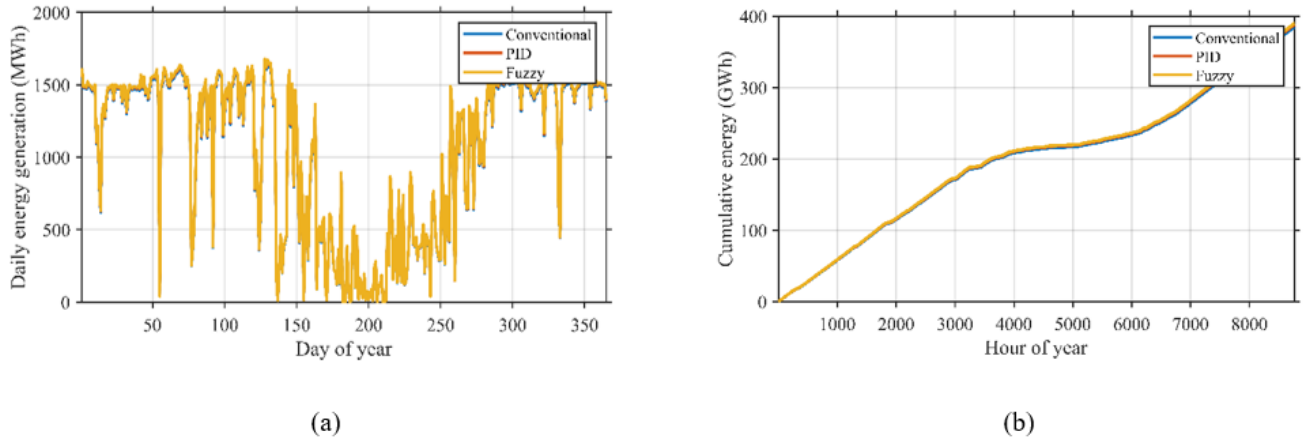


Figure 7. Annual energy comparison: (a) daily electricity generation and (b) cumulative annual electricity generation.

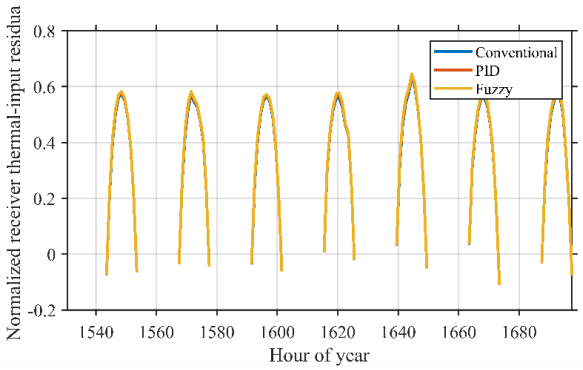


Figure 8. Selected-period normalized residuals for thermal-input receiver positive and negative values are deviations from a 24 h moving trend, the metric is temporal and does not indicate spatial receiver-flux uniformity.

three cases are very close to each other for the study time period and thus do not indicate enhanced receiver stability or an improved spatial flux distribution.

3.6. Paired Daily Statistical Results

All four paired daily tests were significant ($p < 0.001$), as shown in Table 4. The average daily energy was 13.796 MWh day-1 higher for fuzzy supervision than for PID, and the average daily optical efficiency was 0.011385 times higher for fuzzy supervision than for PID. The daily values can be multiplied by 365 to obtain the annual increases in energy and optical efficiency that were reported previously. The large standardized effects indicate that we are dealing with the deterministic separation of post-processed series that were all derived from the same annual dataset. Therefore, these effects should not be used as experimental effect sizes.

3.7. Discussion of Results

In the last comparison between fuzzy and PID supervision, there was a trade-off between the characteristics of the two controllers; thus, neither was clearly better than the other. The fuzzy supervision obtained the highest optical efficiency and highest annual energy savings, whereas the lowest tracking error variability was obtained with the PID supervision. This is because of the supervisory outputs: the fuzzy supervision assigned a much higher tracking authority to the SC than the active-field hours on average, whereas the equal correction coefficients used for the supervision equalized the maximum authorities but not the average control effort.

The modeled fuzzy energy gain of 5.04 GWh yr (-1) was at a plant-relevant scale. However, this post-processing result must be compared with the costs of sensors, drives, communication, calibration, maintenance, actuator electricity, and additional mechanical movement. These penalties have not yet been included in the proposed framework.

In terms of a meaningful comparison between pentagonal and square heliostats of equal area, a number of identical input data would be required. These include field boundaries, tower and receiver dimensions, heliostat spacing rules, weather data, optical errors, ray tracing, structural design, and cost functions. A pentagonal design is a technically interesting option; however, it has not been investigated in previous Stellio studies. These studies have already reported the potential advantages of a complete pentagonal configuration with respect to the layout, kinematics, and structures [5–8] The increase in energy collection of 1.31% by SAM is due to the supervisory model and optical post-processing and therefore cannot be attributed to the pentagonal shape.

The residual of the thermal input at the receiver was for both controllers, and the increase in the selected temporal variability was even larger for the fuzzy controller. To assess receiver-flux uniformity and durability also the spatial receiver-flux maps, the peak flux density, panel-gradients and the thermal-stress analysis have to be presented.

There are a few limitations that must be stated in order to give a correct physical interpretation of the results of this work. First, the angular error was synthetic; that is,

©2026 The Author(s). This article is licensed under CC By 4.0

Table[4]: Paired daily statistical comparison (n = 365)

Comparison	Mean difference	95% CI	p-value	t	Cohen d_z
Fuzzy energy vs conventional energy	13.796 MWh/day	13.126 to 14.467	< 0.001	40.478	2.119
Fuzzy optical efficiency vs conventional	0.011385	0.011246 to 0.011524	< 0.001	161.546	8.456
PID energy vs conventional energy	8.594 MWh/day	8.200 to 8.989	< 0.001	42.825	2.242
PID optical efficiency vs conventional	0.008240	0.008144 to 0.008337	< 0.001	168.147	8.801

it was calculated and not measured during the Al Hudaydah field test. Therefore, it must be verified whether it is correct. Second, hourly sampling was sufficient to perform an annual supervisory control assessment. However, the results could also predict the effects of motor-torque nonlinearity, gearbox backlash, encoder resolution, and second-time-scale behavior of wind turbines under wind fluctuations. Third, the Gaussian optical penalty was approximated using a simple compact relation. However, a more accurate shape-sensitive ray-tracing method would provide a correct optical penalty. Fourth, the TES-preserving power correction only sends a storage-only power update to the TES and does not update the state of charge of the storage in question. In addition, the TES-preserving power correction is not dispatched in the later hours. Fifth, the energy consumption by the controller and mechanical wear were not considered in this study.

All the mentioned angular errors and wind data must be combined with information on the second- to minute time scale behavior of the actuator, the equal-control-effort performance of alternative concepts, a shape-sensitive ray tracing through the telescope pupil, a spatial receiver-flux map, and a dynamically coupled optical-TES-power-block model. The annual differences calculated can only be confirmed by hardware-in-the-loop experiments or field experiments.

3.8. Conclusion

This study compares the Mamdani-type fuzzy supervisory controller (FSC) with conventional control, particularly with the widely used PID controller. The FSC, as well as the PID controller, is tested on a 100 MW plant using a full year of hourly SAM output. The plant consists of a solar tower with a 100 MW gen-set and 8h of storage. The plant is located in Al-Hudaydah, Yemen. A 27-rule fuzzy-supervisory controller was fully tested and compared with PID as well as with several idealized (but unit-consistent) plant models (solar tower only with angular error, with Gaussian optical penalty, etc.). The comparison was performed using a simple TES-preserving power correction in a paired, daily statistical test.

The gain of fuzzy supervision was 5.04 GWh yr-1, or 1.31%. However, the gain of PID control was 4.05 GWh yr-1 or 1.06%, which was higher than that of fuzzy supervision alone. Thus, the annual energy for PID control was 388.05 GWh, which was higher than that for fuzzy supervision. The tracking-error standard deviation of the PID control was 0.01744°, which was the lowest value among the three controllers. While the fuzzy supervision controller produced a 0.42% decrease in the tracking error variability, neither of the supervised controllers produced any decrease in the receiver thermal-input residual metric.

3.9. Declarations

Ethical Approval

This article does not contain any studies involving animals or human participants performed by any of the authors. We declare that this manuscript is original and is not currently considered for publication elsewhere. We further confirm that the order of authors listed in the manuscript has been approved by all of us.

Conflict of interest

The authors declare no competing interests.

Competing interests

The authors have no financial or proprietary interest in any material discussed in this article.

Authors' contributions

All authors contributed to the study conception and design. All authors performed simulations, data collection, and analysis, and commented on the present version of the manuscript. All authors read and approved the final manuscript.

Funding: No funding was received from any organization for this study.

Availability of data and materials

No datasets is used in the present study.

Consent for publication

The authors confirm that informed consent was obtained for the publication of the data contained in this **article.**

Consent to participate

Informed consent was obtained from all authors.

Declaration of AI-Assisted Technologies

"The authors declare that artificial intelligence (AI) tools were used only for limited purposes such as language editing, grammar improvement, and formatting assistance. All scientific content, data analysis, interpretations, conclusions, and final manuscript revisions were

©2026 The Author(s). This article is licensed under CC By 4.0

reviewed and verified by the authors, who took full responsibility for the integrity and originality of the work."

REFERENCES

[1] M. Romero and A. Steinfeld, "Concentrating solar thermal power and thermochemical fuels," *Energy & Environ. Sci.*, vol. 5, no. 11, pp. 9234–9245, 2012. DOI: 10.1039/C2EE21275G

[2] R. P. Merchán, M. J. Santos, A. Medina, and A. Calvo Hernández, "High temperature central tower plants for concentrated solar power: 2021 overview," *Renew. Sustain. Energy Rev.*, vol. 155, no. 111828, 2022. DOI: 10.1016/j.rser.2021.111828

[3] A. N. Yerudkar, D. Kumar, V. H. Dalvi, S. V. Panse, V. R. Gaval, and J. B. Joshi, "Economically feasible solutions in concentrating solar power technology specifically for heliostats - a review," *Renew. Sustain. Energy Rev.*, vol. 189, no. 113825, 2024. DOI: 10.1016/j.rser.2023.113825

[4] S. Wang et al., "Co-optimisation of the heliostat field and receiver for concentrated solar power plants," *Appl. Energy*, vol. 348, no. 121513, 2023. DOI: 10.1016/j.apenergy.2023.121513

[5] T. Keck et al., "High-performance stellio heliostat for high temperature application," in *AIP Conference Proceedings*, vol. 2445, 2022. DOI: 10.1063/5.0086592

[6] F. Arbes, M. Wöhrbach, D. Gebreiter, and G. Weinrebe, "Towards high efficiency heliostat fields," in *AIP Conference Proceedings*, vol. 1850, 2017. DOI: 10.1063/1.4984344

[7] K. Blume, M. Röger, and R. Pitz-Paal, "Full-scale investigation of heliostat aerodynamics through wind and pressure measurements at a pentagonal heliostat," *Sol. Energy*, vol. 251, pp. 337–349, 2023. DOI: 10.1016/j.solener.2022.12.016

[8] K. Blume, M. Röger, and R. Pitz-Paal, "Simplified analytical model to describe wind loads and wind-induced tracking deviations of heliostats," *Sol. Energy*, vol. 256, pp. 96–109, 2023. DOI: 10.1016/j.solener.2023.03.055

[9] M. Chiesi, E. F. Scarselli, and R. Guerrieri, "Run-time detection and correction of heliostat tracking errors," *Renew. Energy*, vol. 105, pp. 702–711, 2017. DOI: 10.1016/j.renene.2016.12.093

[10] M. Pargmann, M. Leibauer, V. Nettelroth, D. Maldonado Quinto, and R. Pitz-Paal, "Enhancing heliostat calibration on low data by fusing robotic rigid body kinematics with neural networks," *Sol. Energy*, vol. 264, no. 111962, 2023. DOI: 10.1016/j.solener.2023.111962

[11] E. Salgado-Plasencia, R. V. Carrillo-Serrano, E. A. Rivas-Araiza, and M. Toledano-Ayala, "Scada-based heliostat control system with a fuzzy logic controller for the heliostat orientation," *Appl. Sci.*, vol. 9, no. 15, p. 2966, 2019. DOI: 10.3390/app9152966

[12] E. H. Mamdani and S. Assilian, "An experiment in linguistic synthesis with a fuzzy logic controller," *Int. J. Man-Machine Stud.*, vol. 7, no. 1, pp. 1–13, 1975. DOI: 10.1016/S0020-7373(75)80002-2

[13] R. Meligy, M. Rady, A. El Samahy, and W. Mohamed, "Proportional-integral-like fuzzy controller of a small-scale linear fresnel reflector solar plant," *IET Renew. Power Gener.*, vol. 14, no. 14, pp. 2620–2628, 2020. DOI: 10.1049/iet-rpg.2020.0024

[14] M. J. Vasallo and J. M. Bravo, "A mpc approach for optimal generation scheduling in csp plants," *Appl. Energy*, vol. 165, pp. 357–370, 2016. DOI: 10.1016/j.apenergy.2015.12.092

[15] K. Kalanithi, G. G. Samuel, M. Malathi, and R. Venkatesan, "Development and implementation of a model predictive control system for a solar parabolic trough plant influenced by an advanced meteorological disturbance model," *Sci. Reports*, vol. 15, p. 36 650, 2025. DOI: 10.1038/s41598-025-20459-y

[16] NASA Langley Research Center, *Prediction of worldwide energy resources (power) data access viewer and hourly api*, NASA POWER Data Services, Accessed: Jul. 2026, 2026.

[17] N. Blair et al., "System advisor model (sam) general description," National Renewable Energy Laboratory, Golden, CO, USA, Tech. Rep. NREL/TP-6A20-70414, 2018, Version 2017.9.5. DOI: 10.2172/1440404

[18] A. Dobos, T. Neises, and M. Wagner, "Advances in csp simulation technology in the system advisor model," *Energy Procedia*, vol. 49, pp. 2482–2489, 2014. DOI: 10.1016/j.egypro.2014.03.263

©2026 The Author(s). This article is licensed under CC By 4.0